

Electronic structures of multilayer graphene quasicrystals

Guodong Yu,^{1,2} Zewen Wu,¹ Zhen Zhan,¹ Mikhail I. Katsnelson,² and Shengjun Yuan^{1,2,*}

¹*Key Laboratory of Artificial Micro- and Nano-structures of Ministry of Education and School of Physics and Technology, Wuhan University, Wuhan 430072, China*

²*Institute for Molecules and Materials, Radboud University, Heijendaalseweg 135, NL-6525 AJ Nijmegen, Netherlands*

In this paper, the electronic properties of several multilayer graphene quasicrystals are studied by means of the tight-binding method. The multilayer graphene quasicrystals are stacked in AA, AB or their combined orders with at least one layer rotated by 30° . The 30° interface introduces the quasi-periodicity by breaking the translational symmetry and separates the layered system into subsystems. Our results indicate that the interactions between subsystems result in the emergence of new van Hove singularities in density of states, new peaks in optical conductivity and strong hybridizations of the eigenstates among subsystems. The periodic approximants of several multilayer graphene quasicrystals are proposed, and their effective band structures are derived by unfolding the band structures of approximants. Our results show that these subsystems are coupled by the interlayer interactions crossing the interface but will retain their own band structures at low-energy region. The band structures of all the subsystems with the same orientation are combined at the corners of the Brillouin zone, and scattered into their mirror-symmetric points inside the Brillouin zone, with weak and anisotropic spectral functions. Such mirror symmetry and combination effects are robust even if an external electric field is applied. Our results suggest that the 30° twisted quasicrystal interface can be used to engineer the band structures of multilayer graphene or other layered two-dimensional materials.

I. INTRODUCTION

In theory, a twisted bilayer graphene (TBG) can transform from a crystalline (commensurate configuration) to quasi-crystalline (incommensurate configuration) depending on the twist angle¹. The commensurate configuration with small twist angle as a model system of strongly correlated electrons has drawn much attention due to the novel electronic properties, such as the flat band^{2,3}, unconventional superconductivity⁴⁻⁶, correlated insulator phases⁷, etc. Recently, the 30° TBG (dodecagonal bilayer graphene quasicrystal), an incommensurate configuration, has been grown successfully on H-SiC(0001)⁸, Pt(111)⁹ and Cu-Ni(111)¹⁰ surfaces. As the first two dimensional quasicrystal based on graphene, 30° TBG has received increasing attention in both experiment and theory¹¹⁻¹⁷. A method to grow high-quality 30° TBG epitaxially on SiC using borazine as a surfactant has been proposed¹¹. A number of Dirac cones, especially the mirror-symmetric ones, were observed by the angle resolved photoemission spectroscopy (ARPES) measurements^{8,9}. The quasicrystalline order in 30° TBG can induce unique localization of electrons without any extrinsic disorders^{12,15}. All these peculiar properties make 30° TBG much different from graphene monolayer, although some studies claimed that TBG with large twist angle ($> 15^\circ$) should behave like two decoupled graphene monolayers^{18,19}.

The twisted multilayer graphenes (TMGs) consist of several subsystems with different orientations, and each subsystem can be graphene monolayer or multilayer. Comparing with the TBG consisting of only graphene monolayer, the electronic properties of TMGs can be tuned by not only twist angle but also stacking order

in subsystems and even electric field. Recently, one kind of TMG, twisted double bilayer graphene (TDBG) consisting of two *AB*-stacked bilayers, has received much attention especially on the properties²⁰⁻²⁴ associated with the strongly correlated electrons in the electrically tunable flat band²⁵⁻²⁸, such as the superconductivity, magnetic phase transition, correlated insulating state, etc. Besides, the *AB-BA* twisted double bilayer graphene under the electric field was found to be a valley Hall insulator.²⁸ A generic TMG, *M*-layer graphene on top of *N*-layer graphene with a twist angle, possesses two topologically nontrivial flat bands, which exhibit a Chern-number hierarchy.²⁹ Similar to the 30° TBG, 30° TMGs, namely multilayer graphene quasicrystals (MGQCs), are expected to possess some striking properties. More importantly, the successful fabrication of 30° TBG and accurate determination of some key structural parameters (such as twist angle, stacking order and interlayer spacing) in experiment^{30,31} ensure the realization of MGQCs in the near future. Therefore, in this paper, we study the effect of the stacking order and electric field on the electronic properties of several MGQCs.

The approximant method is adopted to study the electronic properties of these MGQCs. The method to construct the approximant of 30° TBG¹⁷ still applies to MGQCs. The proposed approximants can be confirmed by comparing their electronic properties, such as the density of states (DOS). So it is necessary to calculate accurately the electronic properties of these MGQCs. However to calculate the electronic properties of a quasicrystal is a big challenge because the band theory is invalid here due to the lack of the translational symmetry in the system. In order to solve the problem, it is a natural idea to simulate these MGQCs by using the large enough

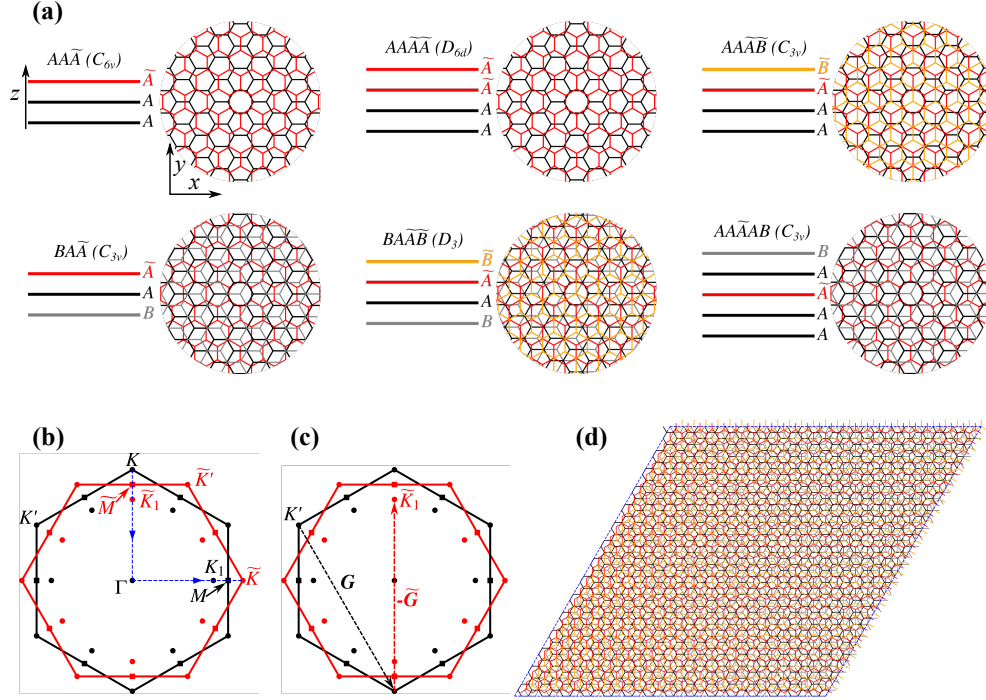


FIG. 1: (a) The multilayer graphene quasicrystals (side and top views) with the point group in bracket. They are named by the sequence of layers from bottom to top. \tilde{A} (red) and \tilde{B} (orange) layers are obtained by rotating A (black) and B (grey) layers by 30° , respectively, so the armchair direction of A and B layers is along the zigzag direction of \tilde{A} and \tilde{B} layers. (b) The Brillouin zones of the 0° - and 30° -subsystems, which are plotted in black and red, respectively. Six \tilde{K}_1 and six K_1 represented by red and black dots inside the Brillouin zones are the mirror-symmetric points of K (and K') and \tilde{K} (and \tilde{K}') points, respectively. (c) Scattering path from K' to \tilde{K}_1 . (d) The elementary unit cell of $15/26$ approximant of $BA\tilde{A}\tilde{B}$. The rotation center is at the four corners. For the $15/26$ approximants of all multilayer graphene quasicrystals, the \tilde{A} and \tilde{B} layers are slightly compressed, which makes the lattice constant change from $a = 2.456 \text{ \AA}$ of a pristine graphene to $\tilde{a} = 2.454 \text{ \AA}$.

round disks, which ensures that the edge states have minor influence on the electronic properties so that they can be ignored safely. In this paper, the round disks with ten million atoms for all MGQCs are adopted. To calculate such big systems is obviously beyond the abilities of density functional theory and even the diagonalization of the tight-binding Hamiltonian due to the enormous CPU time and memory costs. We will use the tight-binding propagation method³² (TBPM) to overcome such computational difficulties. The TBPM is based on the numerical solution of time-dependent Schrödinger equation without any diagonalization, and both memory and CPU costs scale linearly with the system size.

II. METHODS

A. Structures

Each MGQC consists of the 0° - and 30° -subsystems with 0° and 30° standing for the orientations. In this paper, only monolayer, AA or AB stacked bilayers are considered as the subsystem. Besides, the tilde notation is used to distinguish the layers in 30° -subsystems

(\tilde{A} and \tilde{B}) from the layers (A and B) in 0° -subsystems. The schematic diagrams of the MGQCs under study are given in Fig. 1(a). They are named according to the sequence of the layers from bottom to top. Note that the armchair direction of A and B layers is just along the zigzag direction of \tilde{A} and \tilde{B} layers, which results in the quasi-periodicity of these MGQCs due to the absence of the commensurate period. Of all MGQCs under study, only $AAAA$ maintain the D_{6d} point group symmetry of 30° TBG. Adding layer A reduces the symmetry of the system $AAAA$ to C_{6v} due to the loss of the six C_2 rotation axes. But if one layer B or \tilde{B} exists, besides the loss of the C_2 rotation axes, the C_6 rotation axis will change to be C_3 rotation axis, which reduces further the symmetry of the system (BAA , $AA\tilde{A}\tilde{B}$ and $AA\tilde{A}AB$) to C_{3v} . But $BA\tilde{A}\tilde{B}$ has the D_3 point group symmetry due to the recovery of three C_2 rotation axes and the loss of the mirror planes containing C_3 axis. The Brillouin zones (BZs) of 0° - and 30° -subsystems are shown in Fig. 1(b), which are plotted in black and red, respectively. For the MGQCs in Fig. 1(a), the first five structures consist of just one 0° -subsystem and one 30° -subsystem, which are divided by the $A\tilde{A}$ stacking interface. But the last one is

composed of two 0° -subsystems and one 30° -subsystem.

B. Approximants

In order to calculate the electronic properties of these MGQCs, we need to construct the qualified periodic approximants to reproduce accurately the electronic properties of the MGQCs. Then, the EBS corresponding to the primitive unit cell of each layer can be derived by unfolding the band structure of the approximant. The approximant method has been widely used to understand the physics of a quasicrystal³³. In this paper, we follow the procedure proposed for 30° TBG¹⁷ to construct the approximants of all MGQCs. That is, A and B layers keep the lattice constant of a pristine graphene $a = 2.456$ Å, but \tilde{A} and \tilde{B} layers are slightly compressed with the lattice constant changing to be $\tilde{a} = 2.454$ Å, which makes the layers in 0° - and 30° -subsystems the commensurate lattices. The corresponding periodic pattern is used as the approximant, which is named as 15/26 approximant due to the commensurate period $15 \times \sqrt{3}a = 26 \times \tilde{a}$ along the x direction, where $\sqrt{3}a$ and \tilde{a} are the basic periods of A (and B) and \tilde{A} (and \tilde{B}) layers, respectively. Accordingly, the elementary unit cell of the 15/26 approximant contains 1350 atoms in A or B layers and 1352 atoms in \tilde{A} or \tilde{B} layers (see Fig. 1(d)). Our results (shown below) indicate that the 15/26 approximants can reproduce the DOS of these MGQCs accurately. Therefore, the EBSs derived by unfolding the band structures of these 15/26 approximants are reliable, and these 15/26 approximants can be used to further investigate the electronic properties of the MGQCs.

C. Tight-binding model

All MGQCs are simulated by the tight-binding approximation based on p_z orbitals, where the hopping energy between site i and j is³⁴

$$t_{ij} = n^2 V_{pp\sigma}(|\mathbf{r}_{ij}|) + (1 - n^2) V_{pp\pi}(|\mathbf{r}_{ij}|). \quad (1)$$

Here, n is the direction cosine of relative position vector \mathbf{r}_{ij} with respect to \mathbf{e}_z . The Slater and Koster parameters $V_{pp\sigma}$ and $V_{pp\pi}$ have the following form:

$$V_{pp\pi}(|\mathbf{r}_{ij}|) = -\gamma_0 e^{2.218(b-|\mathbf{r}_{ij}|)} F_c(|\mathbf{r}_{ij}|), \quad (2)$$

$$V_{pp\sigma}(|\mathbf{r}_{ij}|) = \gamma_1 e^{2.218(h-|\mathbf{r}_{ij}|)} F_c(|\mathbf{r}_{ij}|). \quad (3)$$

The interlayer distance h and nearest carbon-carbon distance b are 3.349 and 1.418 Å, respectively. γ_0 and γ_1 are 3.12 and 0.48 eV, respectively, which fit well the experimental results of 30° TBG¹⁷. F_c is a smooth function

$$F_c(r) = (1 + e^{(r-0.265)/5})^{-1}. \quad (4)$$

This tight-binding model has been proved by comparing results with several experiments³⁵⁻³⁷. It has been imple-

mented in our home-made code of tight-binding propagation simulator (Tipsi) and reproduces successfully experimentally observed pseudo-magnetic fields in low-angle twisted bilayer graphene³⁷.

D. Tight-binding propagation method

The DOS and optical conductivity are calculated by TBPM³². In TBPM, a random superposition of the p_z orbitals at all sites is used as the initial state $|\phi_0\rangle$ with $\langle\phi_0|\phi_0\rangle = 1$. DOS is calculated as Fourier transform of the time-dependent correlation function

$$d(\epsilon) = \frac{1}{2\pi} \int_{-\infty}^{\infty} e^{i\epsilon\tau} \langle\phi_0|e^{-iH\tau/\hbar}|\phi_0\rangle d\tau. \quad (5)$$

The optical conductivity is calculated by using the Kubo formula in TBPM³². The real part of the optical conductivity matrix $\sigma_{\alpha,\beta}$ at temperature T reads

$$Re\sigma_{\alpha,\beta}(\omega) = \lim_{\epsilon \rightarrow 0^+} \frac{e^{-\hbar\omega/k_B T} - 1}{\hbar\omega A} \int_0^\infty e^{-\epsilon\tau} \sin\omega\tau \times 2Im \langle\phi_2(\tau)|j_\alpha|\phi_1(\tau)\rangle_\beta d\tau. \quad (6)$$

Here, A is the area of the unit cell per layer, and wave functions

$$\begin{aligned} |\phi_1(\tau)\rangle_\beta &= e^{-iH\tau/\hbar} [1 - f(H)] j_\beta |\phi_0\rangle, \\ |\phi_2(\tau)\rangle &= e^{-iH\tau/\hbar} f(H) |\phi_0\rangle, \end{aligned} \quad (7)$$

where $f(H) = 1/(e^{\beta(H-\mu)} + 1)$ is the Fermi-Dirac distribution operator, where μ is the electronic chemical potential.

During the calculations of the DOS and optical conductivity, the MGQCs simulated by a huge enough round disk containing more than 10 million atoms are calculated in TBPM. The elementary unit cell of the 15/26 approximants is repeated to obtain a supercell which contains also 10 million atoms. The open and periodic boundary conditions are applied to the round disk samples and the approximants, respectively. Our results (shown below) indicate that in such large enough system, the edge states have a negligible effect on DOS, but they still have an obvious influence on the optical conductivity for the MGQCs with AA subsystem. Fortunately, the edge states effect doesn't exist in our proposed approximants.

E. Effective band structure

First of all, the spectral function at wavevector \mathbf{k} and energy ϵ can be calculated by³⁸

$$A(\mathbf{k}, \epsilon) = \sum_{I\mathbf{k}_{SC}} P_{I\mathbf{k}_{SC}}(\mathbf{k}) \delta(\epsilon - \epsilon_{I\mathbf{k}_{SC}}), \quad (8)$$

where $\epsilon_{I\mathbf{k}_{SC}}$ is the energy for I^{th} band at wavevector \mathbf{k}_{SC} for the approximant. Actually, only one \mathbf{k}_{SC} , namely

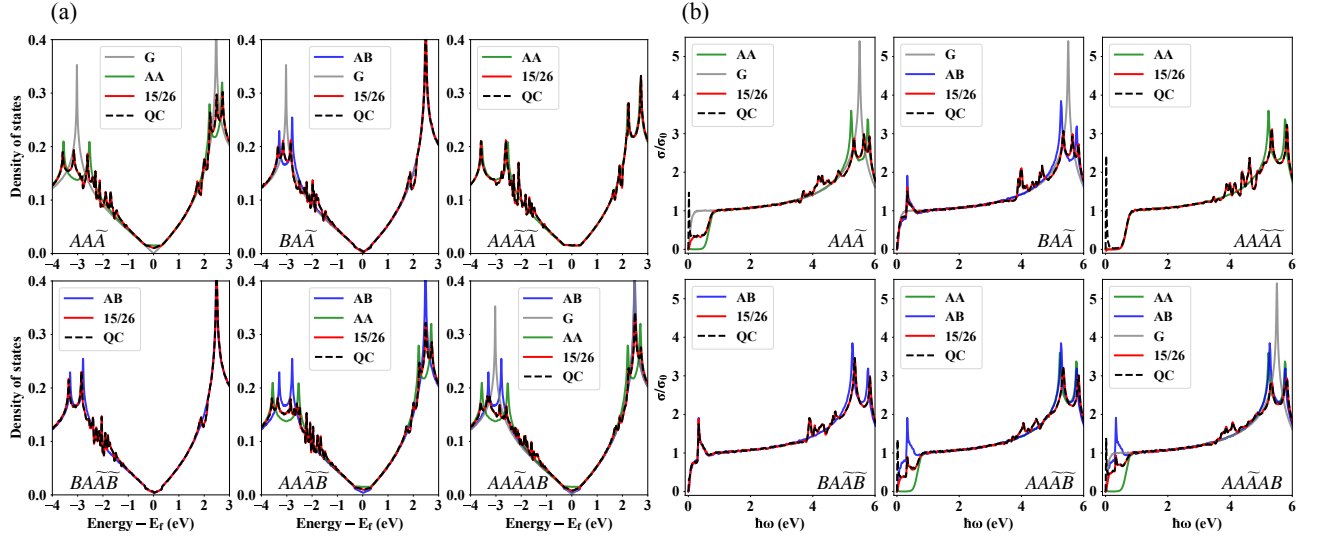


FIG. 2: The comparisons of density of states (a) and real part of optical conductivity (in units of $\sigma_0 = e^2/4h$) (b) among MGQCs (QC), their 15/26 approximants and all subsystems including graphene (G), AA or AB bilayer. Each MGQC contains more than ten million atoms.

$\mathbf{k}_{SC} = \mathbf{k} + \mathbf{G}$ being \mathbf{G} the reciprocal lattice vector of the approximant, contributes to the spectral function. The spectral weight is defined as

$$P_{I\mathbf{k}_{SC}}(\mathbf{k}) = \sum_s \sum_i \left| \langle \psi_{i\mathbf{k}}^{PC_s} | \Psi_{I\mathbf{k}_{SC}}^{SC} \rangle \right|^2 = \sum_s P_{I\mathbf{k}_{SC}}^s(\mathbf{k}), \quad (9)$$

where $|\psi_{i\mathbf{k}}^{PC_s}\rangle$ and $|\Psi_{I\mathbf{k}_{SC}}^{SC}\rangle$ are the eigenstates of layer s and the approximant, respectively. Under the tight-binding method, the spectral weight contributed from layer s can be described by

$$P_{I\mathbf{k}_{SC}}^s(\mathbf{k}) = \frac{1}{n_s} \sum_{\alpha} \sum_{\mathbf{l}_s, \mathbf{l}'_s} e^{i\mathbf{k} \cdot (\mathbf{l}_s - \mathbf{l}'_s)} U_{I\mathbf{k}_{SC}}^{\mathbf{l}_s \alpha*} U_{I\mathbf{k}_{SC}}^{\mathbf{l}'_s \alpha}. \quad (10)$$

Here, n_s is the number of primitive unit cell of layer s in one elementary unit cell of the approximant. $U_{I\mathbf{k}_{SC}}^{\mathbf{l}_s \alpha}$ is the projection of $|\Psi_{I\mathbf{k}_{SC}}^{SC}\rangle$ (the eigenstate of the approximant) on $|\mathbf{k}_{SC} \mathbf{l}_s \alpha\rangle$ (the Bloch basis function of approximant), which can be constructed by all atomic orbitals

$$|\mathbf{k}_{SC} \mathbf{l}_s \alpha\rangle = \frac{1}{N} \sum_{\mathbf{L}} e^{i\mathbf{k}_{SC} \cdot \mathbf{L}} \phi(\mathbf{r} - \mathbf{L} - \mathbf{l}_s - \mathbf{t}_\alpha), \quad (11)$$

where N is a normalization constant, $\phi(\mathbf{r} - \mathbf{L} - \mathbf{l}_s - \mathbf{t}_\alpha)$ is the p_z orbital located at $\mathbf{L} + \mathbf{l}_s + \mathbf{t}_\alpha$. Equation (10) indicates that only the eigenstates of approximant are necessary to obtain the spectral function.

Then, the effective band structure (EBS) can be obtained by³⁹

$$\delta N(\mathbf{k}, \epsilon) = \int_{\epsilon - \delta\epsilon/2}^{\epsilon + \delta\epsilon/2} A(\mathbf{k}, \epsilon') d\epsilon', \quad (12)$$

where $\delta\epsilon$ is the bin width in energy sampling.

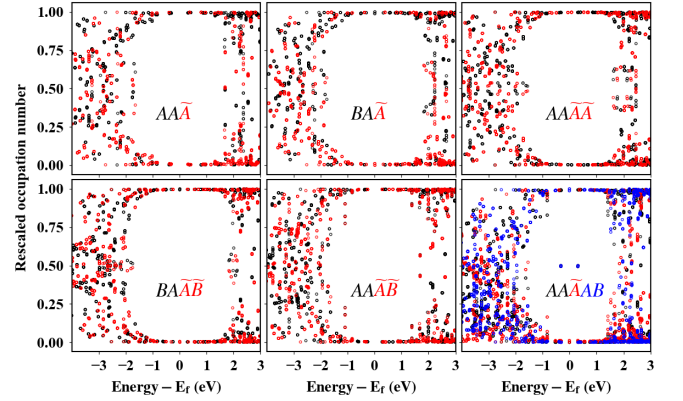


FIG. 3: The rescaled occupation numbers of the eigenstates at Γ point of the 15/26 approximants in the subsystems. Different colors of the rescaled occupation numbers stand for different subsystems.

III. RESULTS AND DISCUSSION

A. DOS and optical conductivity

The DOS and optical conductivity comparisons among the large round disk samples of some MGQCs, their corresponding 15/26 approximants and subsystems are given in Fig. 2. For DOS, which is the counting of states at certain energy, the 15/26 approximants can always reproduce the results of MGQCs. For optical conductivity, which contains the details of the wave function, such as the amplitude and phase distribution in the space, the good agreements between the round disk samples and 15/26 approximants also remain but only for the MGQCs without AA bilayer subsystem. For the MGQCs with

AA bilayer subsystem, the disagreements exist near zero frequency, where there is a big peak for the round disk sample, which can not be reproduced by our 15/26 approximants. Actually, such a big peak originates from the edge states of the AA bilayer subsystem, because such a big peak still exists for the round disk sample of a pristine AA bilayer with open boundary condition (not shown in this paper), but it disappears when applying the periodic boundary condition (see Fig. 2(b)). Therefore, our proposed 15/26 approximants are still accurate to simulate the electronic properties of the infinite MGQCs without boundaries.

For all MGQCs under consideration in this paper, some new van Hove singularities in DOS appear comparing with their corresponding subsystems. Furthermore, these new van Hove singularities results in the appearance of some new peaks in optical conductivities. In order to understand the hybridization between subsystems, we analyze the occupation number differences of the eigenstates between subsystems, which are obtained by diagonalizing the Hamiltonians of the 15/26 approximants. For some MGQCs, such as AAA , BAA and $AA\tilde{A}AB$, the subsystems have large different site numbers, which makes it complicated to analyze the hybridization strength between subsystems using the original definition of the occupation number in subsystem x

$$\rho(x) = \sum_{i \in x} |\phi(i)|^2, \quad (13)$$

which is the summation of the amplitudes of the eigenstate ϕ over all sites i inside the subsystem x . In order to simplify the analysis, we define the rescaled occupation number of an eigenstate by renormalizing the site number of the subsystems as

$$\rho'(x) = \frac{\rho(x)/N_x}{\sum_x \rho(x)/N_x}, \quad (14)$$

where, N_x is the site number in subsystem x . For the MGQC with two subsystems, the rescaled occupation numbers of $[0.5, 0.5]$ and $[0.0, 1.0]$ in the two subsystems correspond to the strongest and weakest hybridizations, respectively, no matter how large different site numbers they have in different subsystems. The calculated rescaled occupation numbers are shown in Fig. 3. It can be found that in the energy regions where the new van Hove singularities appear in the DOS, the hybridization between subsystems are also very strong. But near the Fermi level, the hybridizations are very weak and the DOS is almost the same as its subsystems. All these results indicate that the appearance of these new van Hove singularities originate directly from the hybridizations of the states in different subsystems.

B. Mirror symmetry effect

Firstly, we have a brief review of the electronic structure of the 30° TBG before the discussion of MGQCs.

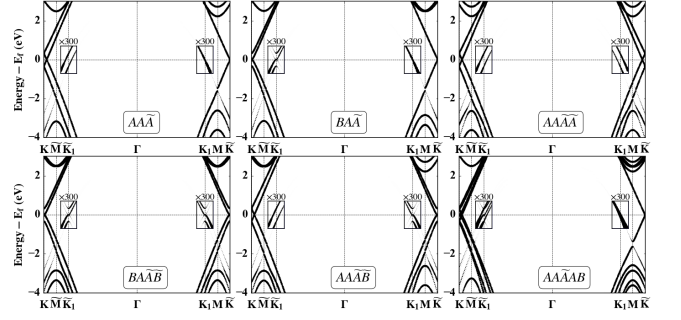


FIG. 4: The effective band structures of the MGQCs with the values enclosed in the rectangles multiplied by 300. The path in k -space is along the arrowed dashed blue line in Fig. 1(b).

Experimental^{8,9} and theoretical studies^{17,40} indicated that, the Dirac cones occur not only at the BZ corners (all K , K' , \tilde{K} and \tilde{K}' points), but also at all their mirror-symmetric points K_1 and \tilde{K}_1 (see Fig. 1(b) for the positions of these points.). This phenomenon can be explained qualitatively by the generalized Umklapp scattering theory^{8,41,42}. Graphene monolayers A and \tilde{A} are crystallines, which have Bloch functions

$$|\mathbf{k}, X\rangle = \frac{1}{\sqrt{n}} \sum_{\mathbf{R}} e^{i\mathbf{k} \cdot \mathbf{R}} |\varphi(\mathbf{r} - \mathbf{R} - \boldsymbol{\tau}_X)\rangle \quad (15)$$

$$|\tilde{\mathbf{k}}, \tilde{X}\rangle = \frac{1}{\sqrt{\tilde{n}}} \sum_{\tilde{\mathbf{R}}} e^{i\tilde{\mathbf{k}} \cdot \tilde{\mathbf{R}}} |\varphi(\mathbf{r} - \tilde{\mathbf{R}} - \boldsymbol{\tau}_{\tilde{X}})\rangle, \quad (16)$$

respectively. The quantities without and with tilde notations correspond to layer A and \tilde{A} respectively. n (\tilde{n}) is the normalization factors, $\boldsymbol{\tau}_X$ ($\boldsymbol{\tau}_{\tilde{X}}$) is the position of sublattice X (\tilde{X}), and $\varphi(\mathbf{r} - \mathbf{R} - \boldsymbol{\tau}_X)$ ($\varphi(\mathbf{r} - \tilde{\mathbf{R}} - \boldsymbol{\tau}_{\tilde{X}})$) is the p_z orbital locating at sublattice X (\tilde{X}) in unit cell \mathbf{R} ($\tilde{\mathbf{R}}$). If the collection of the Bloch functions $\{|\mathbf{k}, X\rangle, |\tilde{\mathbf{k}}, \tilde{X}\rangle\}$ is used as the basis functions of 30° TBG, the interlayer interaction U couples the k state of layer A and \tilde{k} state of layer \tilde{A} , if the condition $\mathbf{k} + \mathbf{G} = \tilde{\mathbf{k}} + \tilde{\mathbf{G}}$ is satisfied, where \mathbf{G} and $\tilde{\mathbf{G}}$ are the reciprocal lattice vectors of A and \tilde{A} layers, respectively. Moreover, the smaller length of $|\mathbf{q}| = |\mathbf{k} + \mathbf{G}|$ corresponds to the stronger scattering (coupling) strength $|\langle \tilde{\mathbf{k}}, \tilde{X} | U | \mathbf{k}, X \rangle|$. The strongest scattering processes scatter the Dirac cones at the K , K' , \tilde{K} and \tilde{K}' to their mirror-symmetric points K_1 and \tilde{K}_1 . As an example, one of the strongest scattering processes for K' point is shown in Fig. 1(c). That is the reason why the Dirac cones exist not only at K , K' , \tilde{K} and \tilde{K}' but also at their mirror-symmetric points K_1 and \tilde{K}_1 .

In order to check whether the mirror symmetry effect still remains in the MGQCs, the EBSs of these MGQCs are shown in Fig. 4. The detailed EBSs around K , K_1 , \tilde{K} and \tilde{K}_1 along four different directions are given in

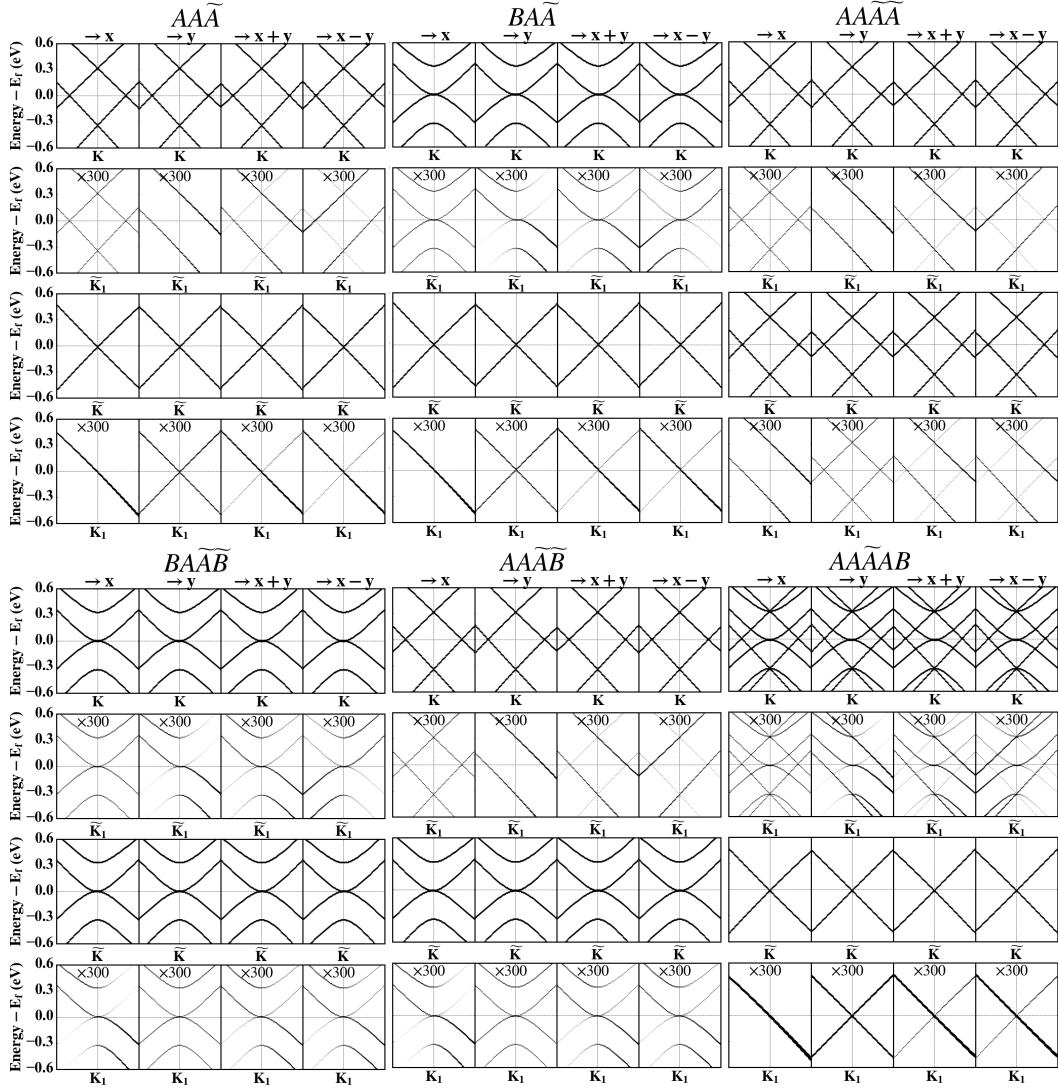


FIG. 5: The effective band structures (EBSs) of the MGQCs around K , K_1 , \tilde{K} and \tilde{K}_1 along four directions x , y , $x + y$ and $x - y$. The EBSs around \tilde{K}_1 and K_1 are multiplied by 300, which are obviously anisotropic along different directions. The mirror symmetry effect, namely the EBSs around \tilde{K}_1 and K_1 being identical to the EBSs around their mirror-symmetric points K and \tilde{K} , respectively, remains for all systems. For the first five systems, the EBSs around K and \tilde{K}_1 (\tilde{K} and K_1) are just the band structures of 0° -subsystem (30° -subsystem). For the case of $AAA\tilde{A}B$, the EBSs at K and \tilde{K}_1 are the combination of the band structures of two 0° -subsystems (AA and AB stacked bilayers), and the EBSs at \tilde{K} and K_1 are the band structure of the 30° -subsystem (the graphene monolayer \tilde{A}).

Fig. 5. Our results show that the EBSs around K_1 and \tilde{K}_1 are always the mirror symmetry of the EBSs at BZ corners (K and \tilde{K}), respectively. Moreover, like 30° TBG¹⁷, the spectral functions at mirror-symmetric points become also anisotropic and much weaker. For any MGQC, the EBSs at \tilde{K}_1 and K_1 are expected to be able to be detected by ARPES measurements because the EBSs of the same magnitude in 30° TBG have been detected successfully^{8,9}.

For the MGQCs composed of only one 0° -subsystem and one 30° -subsystem, for instance, the first five in Fig. 1(a), our results in Fig. 5 indicate that in the low-energy

region the two subsystems always retain their own band structures. For example, in $BAA\tilde{A}$, the EBSs at K and \tilde{K} are just the band structures of AB stacked bilayer graphene and graphene monolayer, which are just the 0° - and 30° -subsystems, respectively. However, different from separating the subsystems in space, the EBSs at BZ corners are always scattered to their mirror-symmetric points. Besides, similar to 30° TBG, the band valleys from any BZ corner (K or \tilde{K}) and its mirror-symmetric point (\tilde{K}_1 or K_1) also hybrid strong near their mid-point (\tilde{M} or M).

The EBSs of the MGQCs in the low-energy region can

also be explained by the generalized Umklapp scattering theory^{41,42}. Let's take $AA\tilde{A}\tilde{B}$ as an example, where the 0° - and 30° -subsystems are AA and $\tilde{A}\tilde{B}$ bilayers, respectively. The Hamiltonian can be written as

$$H = H_A + H_{\tilde{A}} + H_{\tilde{B}} + U_{AA} + U_{A\tilde{A}} + U_{\tilde{A}\tilde{B}} \quad (17)$$

$$= H_{AA} + H_{\tilde{A}\tilde{B}} + U_{A\tilde{A}},$$

where, $H_{AA} = H_A + H_{\tilde{A}} + U_{AA}$ and $H_{\tilde{A}\tilde{B}} = H_{\tilde{A}} + H_{\tilde{B}} + U_{\tilde{A}\tilde{B}}$, which are the Hamiltonians of isolated AA and $\tilde{A}\tilde{B}$ bilayers, respectively. If the collection of the Bloch functions of the two subsystems $\{|\mathbf{k}, X\rangle, |\tilde{\mathbf{k}}, \tilde{X}\rangle\}$ is used as the basis, where X and \tilde{X} are the sublattices of AA and $\tilde{A}\tilde{B}$ bilayers, respectively. H_{AA} and $H_{\tilde{A}\tilde{B}}$ describe the band structures of the AA and AB stacked bilayers after diagonalization, respectively. Then the interaction between the two subsystems $U_{A\tilde{A}}$ as the perturbation scatters the band structures at \tilde{BZ} corners to their mirror-symmetric points.

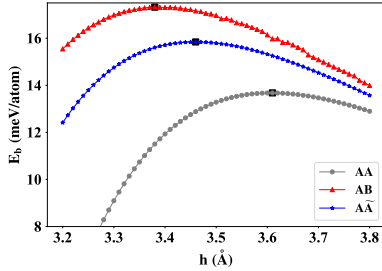


FIG. 6: The binding energies (E_b) at different interlayer distances (h) for AA , AB and $A\tilde{A}$ stackings. They are at the most stable configurations (shown by black squares) when $h = 3.61, 3.38$ and 3.46 Å, where $E_b = 13.7, 17.3$ and 15.8 meV/atom, respectively. For the $A\tilde{A}$ stacking, the round disk with the 12.3 nm radius is used.

Previous calculations^{43–49} indicated that the interlayer binding energies in AB and AA stacked bilayer graphene are $17.7 \sim 70$ and $10.4 \sim 31.1$ meV/atom, respectively, depending on the calculation method. The binding energy in 30° TBG is 1.6 meV/atom smaller than that in the AB stacking⁹. In order to compare the relative stabilities among the three stackings quantitatively and clearly, the binding energies should be calculated in the same method. In this paper, they are calculated by the classical molecular simulations. The intra- and interlayer interactions are described by classical REBO⁵⁰ and Kolmogorov-Crespi⁵¹ potentials, which are implemented in the LAMMPS software⁵². For a fixed interlayer spacing, the atoms are allowed to move only in xy plane. The binding energies of the three stackings at different interlayer spacings are shown in Fig. 6. Our results show that the binding energies in AB , AA and $A\tilde{A}$ stackings are 17.3, 13.7 and 15.8 meV/atom respectively. So $A\tilde{A}$ is less stable than AB stacking, but still more stable than AA stacking. As a consequence, in principle, for the MGQC,

it is not definitely convincing to treat the interlayer interaction across $A\tilde{A}$ stacking interface as a perturbation when comparing with the AA stacking interface. However, all of our calculated EBSs of the MGQCs indicate that, comparing with the AA and AB stacking interfaces, to treat the interlayer interaction across the $A\tilde{A}$ stacking interface as the perturbation can always give the accurate band structure in the low-energy region.

C. Under the electric field

Because the band structure of the subsystem in MGQCs, such as AA and AB stacked bilayers, is sensitive to the electric field, the application of the electric field is expected to be a valid method to turn the EBSs of the MGQCs. The calculated EBSs of the MGQCs under the 0.05 eV/Å electric field along z direction are shown in Fig. 7. The results indicate that in the low-energy region all subsystems still perform like isolated systems and keep their own band structures at the BZ corners. For instance, in $AA\tilde{A}\tilde{B}$, the EBSs at K and \tilde{K} are just the band structures of the 0° - and 30° -subsystems, namely the AA and AB stacked bilayers, respectively, under an external electric field. Importantly, the mirror symmetry effect of the EBS still remains. Therefore, relative to the AA and AB stacking interfaces, it is still reliable to deal with the interlayer interaction across the $A\tilde{A}$ stacking interface as the perturbation even under the electric field. Besides, the charge transfer from top to bottom subsystem can be obviously detected from these calculated EBSs after the application of the electric field, which results in the p- and n-type doping in two subsystems, respectively. Although the screen effect are not included in our calculations, the weaker charge transfer should still exist. Therefore, the application of the electric field is an effective method to engineer the EBSs of MGQCs due to the multilayer structure of the subsystems.

D. Combination effect

For the MGQC composed of two 0° -subsystems and one 30° -subsystem, namely $AA\tilde{A}\tilde{A}B$. The two 0° -subsystems, AB and AA stacked bilayers, share the same BZ (the black one in Fig. 1(b)). The 30° -subsystem is a graphene monolayer \tilde{A} , whose BZ is the red one in Fig. 1(b). The result shown in Fig. 5(f) indicates that the EBS around K is the combination of the band structures of the AA and AB stacked bilayers, which is also scattered to \tilde{K}_1 . Such a result opens up a way to engineer the band structure of the graphene multilayer. If the combination of the band structures of two different structures is required, we can replace the two 0° -subsystems with corresponding structures. For example, if the two 0° -subsystems are replaced with graphene and AA stacked bilayer graphene, namely $AA\tilde{A}A$, the combination of

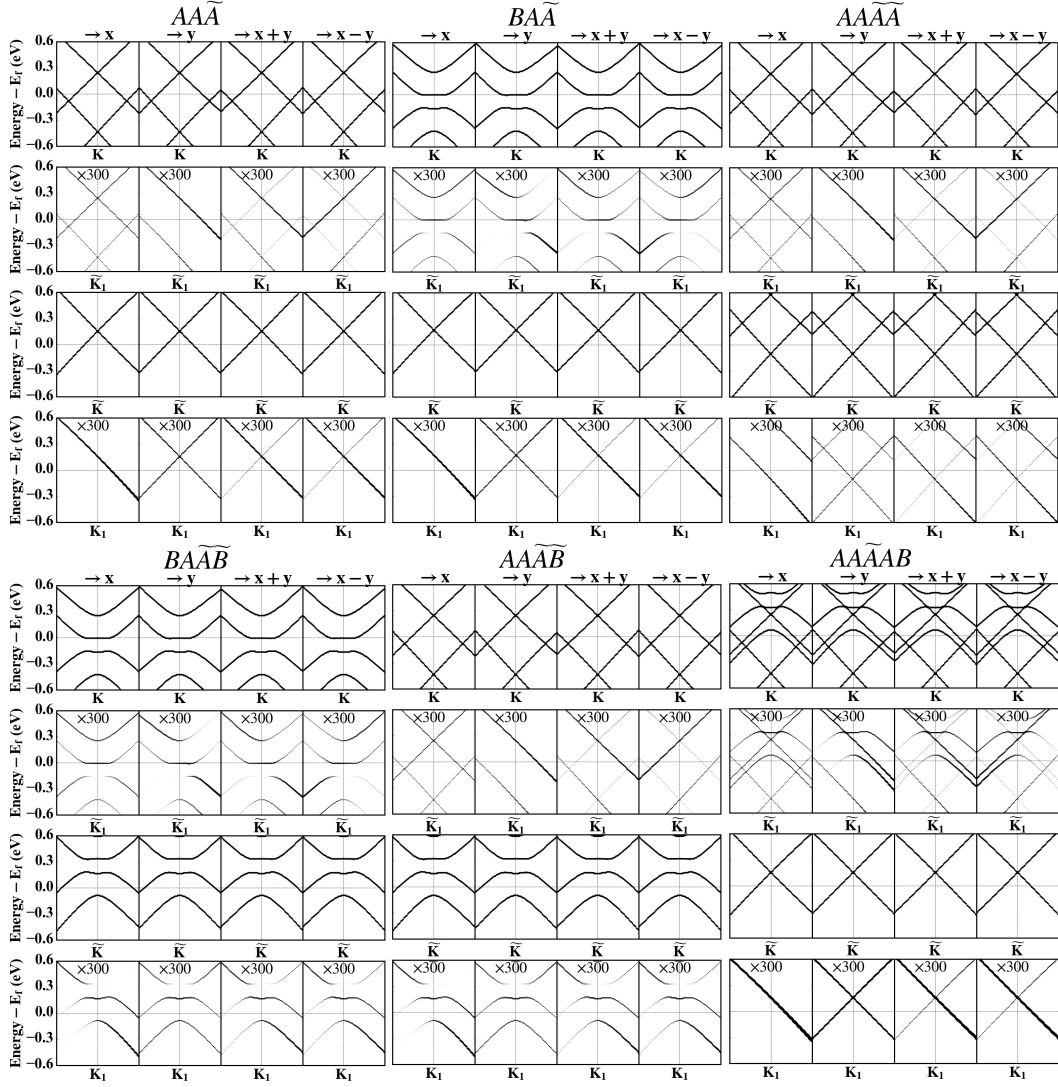


FIG. 7: The effective band structures (EBs) of MGQCs under the electric field of 0.05 eV/\AA around K , K_1 , \tilde{K} and \tilde{K}_1 along four directions x , y , $x+y$ and $x-y$. The EBs around \tilde{K}_1 and K_1 are multiplied by 300. The mirror symmetry effect still remains. For the first five systems, the EBs around K and \tilde{K}_1 (\tilde{K} and K_1) are the band structures of the 0° -subsystem (30° -subsystem) under the electric field with extra electrons (holes) doping. For the case of $AAAAB$, the EBs at K and \tilde{K}_1 are the combination of the band structures of AA and AB stacked bilayers under the electronic field with extra electrons and holes doping, respectively, and the EBs at \tilde{K} and K_1 are the band structure of p-type doped graphene monolayer.

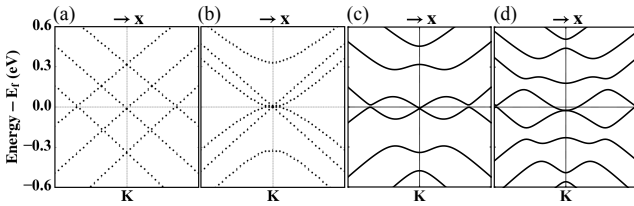


FIG. 8: The effective band structures of AAA (a) and $BAAA$ (b) and the band structures of AAB (c) and $AAAB$ (d) around K along x direction.

graphene occurs at K point (see Fig. 8(a)). For $BAAA$, the EBS at K point is the combination of the band structures of graphene and AB stacked bilayer graphene (see Fig. 8(b)). Such a strategy can also be verified by comparing the EBS of $AAAAB$ with the band structures of AAB and $AAAB$, both of which are crystalline. All the three structures contain both AA and AB stacking interfaces. However, the interactions among the layers in AAB and $AAAB$ make the band structures totally different from the combination of the band structures of AA and AB stacked bilayers (see Fig. 8). Besides, if the distance between the two middle layers in $AAAB$ is increased to be large enough, the band structure of the

the band structures of graphene and AA stacked bilayer

system would show the combination, while these two bilayers are separated totally in not only structure but also electronic properties.

The EBS of a general MGQC composed of several 0° - and 30° -subsystems can be envisioned. According to our calculated EBSs of the MGQCs with one and two subsystems with the same orientation, it can be expected that each subsystem in the general MGQC should keep its own band structure in the low-energy region at the BZ corners. Accordingly, the combination of the band structures of all 0° - and 30° -subsystems should appear at corresponding BZ corners. Moreover, these EBSs should be scattered into the their each six mirror-symmetric points, respectively.

IV. CONCLUSION

By means of the tight-binding approximation, we systematically study the electronic properties of some multilayer graphene quasicrystals (MGQCs), which are composed of some subsystems, such as graphene monolayer, AA and AB stacked bilayer graphenes, with some of the subsystems twisted by 30° . Comparing with these subsystems, some new van Hove singularities and peaks appear in DOS and optical conductivity, respectively, due to the interactions between subsystems. Moreover, the eigenstates show strong hybridization between the subsystems in the energy regions where the new van Hove singularities appear in DOS. By comparing with the DOS

and optical conductivity of the round disk samples containing 10 million sites, the approximants of six MGQCs are proposed. Then, the effective band structures of these MGQCs are derived by using the band-unfolding method. The band structures of all subsystems with the same orientation are combined at the corners of the Brillouin zone, and scattered into their mirror-symmetric points inside the Brillouin zone, with weak and anisotropic spectral functions. Such mirror symmetry and combination effects are robust even if an external electric field is applied. The mirror symmetry and combination effects in MGQC open up a way to engineer the band structure of graphene multilayers.

ACKNOWLEDGEMENTS

This work is supported by the National Science Foundation of China (Grant No. 11774269) and China Postdoctoral Science Foundation (Grant No. 2018M632902). MIK acknowledges a support by the JTC-FLAGERA Project GRANSPORT. Numerical calculations presented in this paper have been partially performed on the supercomputing system in the Supercomputing Center of Wuhan University. Support by the Netherlands National Computing Facilities foundation (NCF), with funding from the Netherlands Organisation for Scientific Research (NWO), is gratefully acknowledged.

* Electronic address: s.yuan@whu.edu.cn

- ¹ S. Shallcross, S. Sharma, E. Kandelaki, and O. A. Pankratov, *Phys. Rev. B* **81**, 165105 (2010).
- ² E. Suárez Morell, J. D. Correa, P. Vargas, M. Pacheco, and Z. Barticevic, *Phys. Rev. B* **82**, 121407 (2010).
- ³ R. Bistritzer and A. H. MacDonald, *Proceedings of the National Academy of Sciences* **108**, 12233 (2011).
- ⁴ Y. Cao, V. Fatemi, S. Fang, K. Watanabe, T. Taniguchi, E. Kaxiras, and P. Jarillo-Herrero, *Nature* **556**, 43 (2018), article.
- ⁵ H. C. Po, L. Zou, A. Vishwanath, and T. Senthil, *Phys. Rev. X* **8**, 031089 (2018).
- ⁶ M. Yankowitz, S. Chen, H. Polshyn, Y. Zhang, K. Watanabe, T. Taniguchi, D. Graf, A. F. Young, and C. R. Dean, *Science* **363**, 1059 (2019).
- ⁷ Y. Cao, V. Fatemi, A. Demir, S. Fang, S. L. Tomarken, J. Y. Luo, J. D. Sanchez-Yamagishi, K. Watanabe, T. Taniguchi, E. Kaxiras, R. C. Ashoori, and P. Jarillo-Herrero, *Nature* **556**, 80 (2018).
- ⁸ S. J. Ahn, P. Moon, T.-H. Kim, H.-W. Kim, H.-C. Shin, E. H. Kim, H. W. Cha, S.-J. Kahng, P. Kim, M. Koshino, Y.-W. Son, C.-W. Yang, and J. R. Ahn, *Science* **361**, 782 (2018).
- ⁹ W. Yao, E. Wang, C. Bao, Y. Zhang, K. Zhang, K. Bao, C. K. Chan, C. Chen, J. Avila, M. C. Asensio, J. Zhu, and S. Zhou, *Proceedings of the National Academy of Sciences* **115**, 6928 (2018).

- ¹⁰ Y. Takesaki, K. Kawahara, H. Hibino, S. Okada, M. Tsuji, and H. Ago, *Chemistry of Materials* **28**, 4583 (2016).
- ¹¹ Y. R. Lin, N. Samiseresht, M. Franke, S. Parhizkar, S. Soubatch, B. Amorim, T. L. Lee, C. Kumpf, F. S. Tautz, and F. C. Bocquet, *arXiv e-prints*, arXiv:1809.07958 (2018).
- ¹² M. J. Park, H. S. Kim, and S. Lee, *Phys. Rev. B* **99**, 245401 (2019).
- ¹³ E. Koren and U. Duerig, *Phys. Rev. B* **93**, 201404 (2016).
- ¹⁴ T. Suzuki, T. Iimori, S. J. Ahn, Y. Zhao, M. Watanabe, J. Xu, M. Fujisawa, T. Kanai, N. Ishii, J. Itatani, K. Suwa, H. Fukidome, S. Tanaka, J. R. Ahn, K. Okazaki, S. Shin, F. Komori, and I. Matsuda, *ACS Nano* **13**, 11981 (2019).
- ¹⁵ P. Moon, M. Koshino, and Y.-W. Son, *Phys. Rev. B* **99**, 165430 (2019).
- ¹⁶ C. Yan, D. Ma, J. Qiao, H. Zhong, L. Yang, S.-Y. Li, Z. Fu, Y. Zhang, and L. He, *2D Materials* (2019).
- ¹⁷ G. Yu, Z. Wu, Z. Zhan, M. I. Katsnelson, and S. Yuan, *npj Computational Materials* **5**, 122 (2019).
- ¹⁸ J. Hass, F. Varchon, J. E. Millán-Otoya, M. Sprinkle, N. Sharma, W. A. de Heer, C. Berger, P. N. First, L. Magaud, and E. H. Conrad, *Phys. Rev. Lett.* **100**, 125504 (2008).
- ¹⁹ M. Sprinkle, D. Siegel, Y. Hu, J. Hicks, A. Tejeda, A. Taleb-Ibrahimi, P. Le Fèvre, F. Bertran, S. Vizzini, H. Enriquez, S. Chiang, P. Soukiassian, C. Berger, W. A. de Heer, A. Lanzara, and E. H. Conrad, *Phys. Rev. Lett.*

- 103**, 226803 (2009).
- ²⁰ X. Liu, Z. Hao, E. Khalaf, J. Y. Lee, K. Watanabe, T. Taniguchi, A. Vishwanath, and P. Kim, arXiv e-prints , arXiv:1903.08130 (2019).
 - ²¹ Y. Cao, D. Rodan-Legrain, O. Rubies-Bigordà, J. M. Park, K. Watanabe, T. Taniguchi, and P. Jarillo-Herrero, arXiv e-prints , arXiv:1903.08596 (2019).
 - ²² M. S. Scheurer, R. Samajdar, and S. Sachdev, arXiv e-prints , arXiv:1906.03258 (2019).
 - ²³ C. Shen, N. Li, S. Wang, Y. Zhao, J. Tang, J. Liu, J. Tian, Y. Chu, K. Watanabe, T. Taniguchi, R. Yang, Z. Y. Meng, D. Shi, and G. Zhang, arXiv e-prints , arXiv:1903.06952 (2019).
 - ²⁴ G. W. Burg, J. Zhu, T. Taniguchi, K. Watanabe, A. H. MacDonald, and E. Tutuc, Phys. Rev. Lett. **123**, 197702 (2019).
 - ²⁵ F. Haddadi, Q. Wu, A. J. Kruchkov, and O. V. Yazyev, arXiv e-prints , arXiv:1906.00623 (2019).
 - ²⁶ N. R. Chebrolov, B. L. Chittari, and J. Jung, Phys. Rev. B **99**, 235417 (2019).
 - ²⁷ Y. W. Choi and H. J. Choi, Phys. Rev. B **100**, 201402 (2019).
 - ²⁸ M. Koshino, Phys. Rev. B **99**, 235406 (2019).
 - ²⁹ J. Liu, Z. Ma, J. Gao, and X. Dai, Phys. Rev. X **9**, 031021 (2019).
 - ³⁰ L. Brown, R. Hovden, P. Huang, M. Wojcik, D. A. Muller, and J. Park, Nano Letters **12**, 1609 (2012).
 - ³¹ J.-B. Wu, H. Wang, X.-L. Li, H. Peng, and P.-H. Tan, Carbon **110**, 225 (2016).
 - ³² S. Yuan, H. De Raedt, and M. I. Katsnelson, Phys. Rev. B **82**, 115448 (2010).
 - ³³ A. I. Goldman and R. F. Kelton, Rev. Mod. Phys. **65**, 213 (1993).
 - ³⁴ J. C. Slater and G. F. Koster, Phys. Rev. **94**, 1498 (1954).
 - ³⁵ G. Trambly de Laissardière, D. Mayou, and L. Magaud, Phys. Rev. B **86**, 125413 (2012).
 - ³⁶ L. Huder, A. Artaud, T. Le Quang, G. T. de Laissardière, A. G. M. Jansen, G. Lapertot, C. Chapelier, and V. T. Renard, Phys. Rev. Lett. **120**, 156405 (2018).
 - ³⁷ H. Shi, Z. Zhan, Z. Qi, K. Huang, E. van Veen, J. A. Silva-Guillén, R. Zhang, P. Li, K. Xie, H. Ji, M. I. Katsnelson, S. Yuan, S. Qin, and Z. Zhang, arXiv e-prints , arXiv:1905.04515 (2019).
 - ³⁸ H. Nishi, Y.-i. Matsushita, and A. Oshiyama, Phys. Rev. B **95**, 085420 (2017).
 - ³⁹ P. V. C. Medeiros, S. Stafström, and J. Björk, Phys. Rev. B **89**, 041407 (2014).
 - ⁴⁰ F. Rost, R. Gupta, M. Fleischmann, D. Weckbecker, N. Ray, J. Olivares, M. Vogl, S. Sharma, O. Pankratov, and S. Shallcross, Phys. Rev. B **100**, 035101 (2019).
 - ⁴¹ M. Koshino and P. Moon, Journal of the Physical Society of Japan **84**, 121001 (2015).
 - ⁴² M. Koshino, New Journal of Physics **17**, 015014 (2015).
 - ⁴³ E. Mostaani, N. D. Drummond, and V. I. Fal'ko, Phys. Rev. Lett. **115**, 115501 (2015).
 - ⁴⁴ S. D. Chakarova-Käck, E. Schröder, B. I. Lundqvist, and D. C. Langreth, Phys. Rev. Lett. **96**, 146107 (2006).
 - ⁴⁵ I. V. Lebedeva, A. A. Knizhnik, A. M. Popov, Y. E. Lozovik, and B. V. Potapkin, Phys. Chem. Chem. Phys. **13**, 5687 (2011).
 - ⁴⁶ Y. J. Dappe, P. G. Bolcatto, J. Ortega, and F. Flores, Journal of Physics: Condensed Matter **24**, 424208 (2012).
 - ⁴⁷ R. Podeszwa, The Journal of Chemical Physics **132**, 044704 (2010).
 - ⁴⁸ T. Gould, S. Lebègue, and J. F. Dobson, Journal of Physics: Condensed Matter **25**, 445010 (2013).
 - ⁴⁹ W. Gao and A. Tkatchenko, Phys. Rev. Lett. **114**, 096101 (2015).
 - ⁵⁰ D. W. Brenner, O. A. Shenderova, J. A. Harrison, S. J. Stuart, B. Ni, and S. B. Sinnott, Journal of Physics: Condensed Matter **14**, 783 (2002).
 - ⁵¹ A. N. Kolmogorov and V. H. Crespi, Phys. Rev. B **71**, 235415 (2005).
 - ⁵² S. Plimpton, Journal of Computational Physics **117**, 1 (1995).